PNAS RESEARCH ARTICLE | BIOCHEMISTRY BIOPHYSICS AND COMPUTATIONAL BIOLOGY OPEN ACCESS

Enhanced incorporation of subnanometer tags into cellular proteins for fluorescence nanoscopy via optimized genetic code expansion

Tiberiu S. Mihaila[a,1], Carina Bäte[a], Lynn M. Ostersehlt[a], Jasmin K. Pape[a], Jan Keller-Findeisen[a], Steffen J. Sahl[a], Stefan W. Hell[a,b,2]

Contributed by Stefan W. Hell; received February 2, 2022; accepted May 27, 2022; reviewed by Edward Lemke and Dieter Söll

With few-nanometer resolution recently achieved by a new generation of fluorescence nanoscopes (MINFLUX and MINSTED), the size of the tags used to label proteins will increasingly limit the ability to dissect nanoscopic biological structures. Bioorthogonal (click) chemical groups are powerful tools for the specific detection of biomolecules. Through the introduction of an engineered aminoacyl–tRNA synthetase/tRNA pair (tRNA: transfer ribonucleic acid), genetic code expansion allows for the site-specific introduction of amino acids with "clickable" side chains into proteins of interest. Well-defined label positions and the subnanometer scale of the protein modification provide unique advantages over other labeling approaches for imaging at molecular-scale resolution. We report that, by pairing a new N-terminally optimized pyrrolysyl–tRNA synthetase (chPylRS$_{2020}$) with a previously engineered orthogonal tRNA, clickable amino acids are incorporated with improved efficiency into bacteria and into mammalian cells. The resulting enhanced genetic code expansion machinery was used to label β-actin in U2OS cell filopodia for MINFLUX imaging with minimal separation of fluorophores from the protein backbone. Selected data were found to be consistent with previously reported high-resolution information from cryoelectron tomography about the cross-sectional filament bundling architecture. Our study underscores the need for further improvements to the degree of labeling with minimal-offset methods in order to fully exploit molecular-scale optical three-dimensional resolution.

nanoscopy | genetic code expansion | fluorescence | click chemistry | actin

Significance

Systematic optimization of a pyrrolysyl–tRNA synthetase pair (tRNA: transfer ribonucleic acid) is shown to improve the incorporation of clickable amino acids into structured regions of proteins, in both bacterial and mammalian cells. The enhanced labeling of target proteins is demonstrated in fluorescence nanoscopy experiments of β-actin. MINFLUX measurements of filopodia at ∼2-nm three-dimensional precision contain segments with localization patterns that are consistent with a triangular filament bundling pattern, featuring interfilament separations close to 12 nm, that was previously only accessible via cryogenic imaging methods. This study highlights the potential of molecular-scale fluorescence nanoscopies when paired with minimally displacing labeling tags.

Fluorescence imaging techniques have become indispensable tools for exploring the in situ spatial organizations and compositions of cellular structures. As resolution has improved, increasingly intricate biological observations have become possible (1). A major leap was made when superresolution fluorescence microscopes began to discern molecules spaced much closer than the ∼200-nm resolution limit imposed by diffraction of light (2–5). Routinely realizing 20- to 40-nm resolution, fluorescence nanoscopy methods like STED, PALM and STORM have allowed for the characterization of many cellular assemblies (6–8). Recently, major new advancements were reported with MINFLUX (9) and MINSTED (10), nanoscopy approaches that combine principles from coordinate-targeted approaches like STED with those from coordinate-stochastic single-molecule-based methods, like PALM/STORM. Outperforming established superresolution methods by 10-fold, MINFLUX localizes fluorophores with three-dimensional (3D) precisions <3 nm (SD) in biological samples, i.e., at length scales equal to or smaller than the size of commonly used labeling tags (11–13).

Antibodies, fluorescent proteins, and self-labeling (enzymatic) protein tags, such as SNAP-tag, Halo-tag, and CLIP-tag (14–16), have been used to specifically label proteins with fluorophores for a variety of superresolution methods. However, each of these labeling approaches introduces an offset between the target biomolecule and the fluorescent label, limiting the accuracy with which the imaging measurement represents the biological structure in question. Furthermore, given that biological assemblies have multiple molecules, labeling errors (ε) will often manifest in opposing directions, doubling the effect of the tag offset on the measurement (Fig. 1*A*). To measure small structures with minimal artifacts, both high localization precisions and low labeling errors are needed (Fig. 1*B*).

For each antibody used, fluorophores are offset from the target protein by an average of ∼10 nm. Furthermore, the flexibility of the antibodies can lead to inconsistent labeling errors between molecules within the same structure (17). Protein tags introduce around 3 nm of separation from the N or C terminus of the tagged protein. These terminal regions are themselves unstructured and flexible in many proteins (18, 19), introducing additional uncertainty and often separation from structured regions. The magnitudes of

Author contributions: T.S.M. designed research; T.S.M., C.B., L.M.O., and J.K.P. performed research; T.S.M. and J.K.-F. analyzed data; L.M.O. and J.K.P. performed MINFLUX nanoscopy; S.J.S. and S.W.H. provided guidance on MINFLUX imaging throughout the project; and T.S.M., S.J.S., and S.W.H. wrote the paper.

Reviewers: E.L., Johannes Gutenberg University of Mainz; D.S., Yale University.

Competing interest statement: The Max Planck Society holds patents on selected embodiments and procedures of MINFLUX, benefitting S.W.H.

[1]Present address: Columbia University, Vagelos College of Physicians and Surgeons, New York, NY 10032.

[2]To whom correspondence may be addressed. Email: stefan.hell@mpinat.mpg.de.

This article contains supporting information online at http://www.pnas.org/lookup/suppl/doi:10.1073/pnas.2201861119/-/DCSupplemental.

Published July 13, 2022.

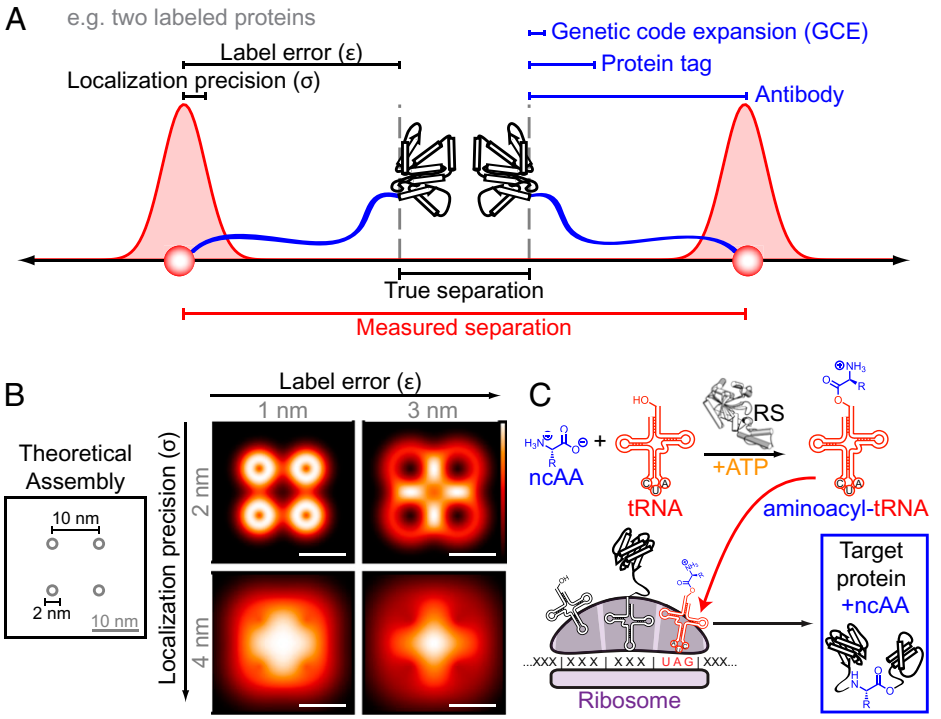

Fig. 1. Concepts behind pairing MINFLUX with genetic code expansion. (*A*) Offsets between the fluorescent labels and target biomolecules can compromise the accuracy with which a measurement reflects the underlying structure, particularly given the molecular-scale localization precisions achieved by MINFLUX. (*B*) Simulated molecular assembly illustrating how different combinations of precision and label error can produce different measured patterns. (Scale bar: 10 nm.) (*C*) In genetic code expansion, an engineered tRNA and RS are introduced. The RS will specifically conjugate a ncAA to the new tRNA, which has an anticodon that corresponds to a stop codon, typically amber (5′-UAG-3′). If a single mutation is introduced to the protein of interest that exchanges a sense codon for the amber codon, the ribosome will insert the ncAA from the aminoacyl-tRNA into the protein at that site.

such systemic inaccuracies are large enough to limit the biological information extracted from the (sub)nanometer localization precision provided by MINFLUX. In fact, fluorophore-to-target separations have been shown to impact measurements obtained with established superresolution methods as well (20–22). Furthermore, the bulk from large tags on protein termini can modify or disrupt protein function and dynamics (23–26). To fully maximize the information extracted from MINFLUX measurements, a labeling approach should be used that introduces minimally disruptive protein labels that are subnanometer in size and that can be specifically introduced into structured regions of proteins.

Genetic code expansion (GCE) is a promising method that meets these requirements. In GCE, an amino acid with a unique nonnatural side chain, a noncanonical amino acid (ncAA), is site-specifically incorporated into the sequence of a protein of interest (27). These modified side chains are typically equally as long as (or only a few atoms longer than) those of the amino acids naturally found in proteins (28). For site-specific protein labeling, ncAAs have been developed, which feature special chemical groups that can react bioorthogonally, i.e., these moieties will specifically react with their partners without labeling the chemical groups that are naturally found in biological molecules. To genetically incorporate clickable amino acids into proteins in living cells, an engineered tRNA (transfer ribonucleic acid) and aminoacyl–tRNA synthetase (RS) must be introduced to cells, allowing for introduction of the ncAA at a nonsense (stop) mutation substituted into the target molecule's sequence (Fig. 1*C*).

ncAAs for the major click reactions (29–32) have been genetically incorporated through engineered machinery from *Methanosarcina barkeri* and *Methanosarcina mazei* (*Mb* and *Mm*, respectively), the organisms of which naturally use an additional amino acid called pyrrolysine (Pyl). Such tRNA/RS pairs have been used to introduce clickable ncAAs into a variety of targets and organisms, even allowing for superresolution imaging in some cases (33–35).

To achieve high signal-to-background ratio in fluorescence microscopy, it is desirable to use a tRNA/RS pair that incorporates clickable amino acids as efficiently as possible (33, 36). Mutations in the tRNA and the RS have been shown to improve the efficiencies of pyrrolysyl GCE pairs both in bacteria and in mammalian cells (Fig. 2*A*).

By combining a recently reported tRNA with a reengineered pyrrolysyl synthetase featuring a set of mutations in the N-terminal domain, we arrived at a pair that improved the incorporation of clickable amino acids by severalfold in both mammalian and bacterial cells. The pair provides substantially higher fluorescence imaging signal when compared to existing GCE pairs. This GCE machinery was used for superresolution imaging of the actin cytoskeleton, resolving details about the 3D assembly of actin filaments in filopodia with MINFLUX nanoscopy.

Results

Testing a Previously Optimized RS with an Engineered tRNA. The pyrrolysyl-tRNA/RS system was chosen due to established compatibility with major click chemistry groups and due to the unique two-domain structure of PylRS. The C-terminal domain of the enzyme contains the amino acid binding pocket while the N-terminal domain is responsible for facilitating binding to the tRNA. Thus, mutations can be made in the N-terminal domain to optimize the tRNA/RS interaction without affecting the shape of the amino acid binding pocket, preserving the enzyme's specificity for ncAAs.

A particularly efficient RS with N-terminal mutations emerged from continuous evolution of a chimeric RS. Four

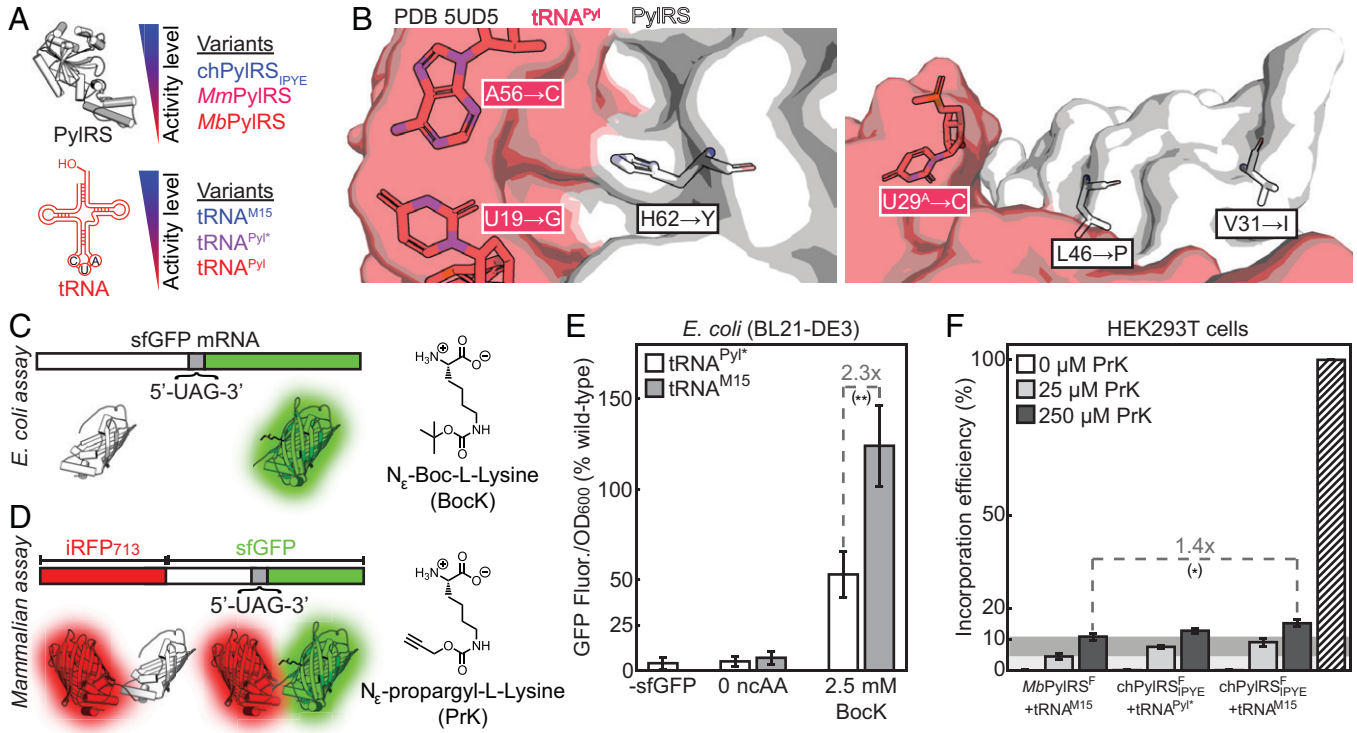

Fig. 2. The orthogonal tRNA^{M15} is compatible with the highly efficient chPylRS$_{IPYE}$ enzyme, substantially improving incorporation efficiency in *E. coli,* compared to the previously used tRNA^{Pyl*}. Bars in plots represent the mean of three biological replicates and error bars show SD between biological replicates. *P < 0.05, **P < 0.01 (see *SI Appendix*, section S14 for exact P values). (*A*) Several variants of *Methanosarcina* PylRS enzymes and of orthogonal tRNAs have been used for genetic code expansion, but the highly efficient chPylRS$_{IPYE}$ enzyme has not been paired with a recently reported enhanced orthogonal tRNA (tRNA^{M15}). (*B*) Analysis of a published crystal structure shows that the resolved residues mutated in chPylRS$_{IPYE}$ do not interact with any nucleobases modified in tRNA^{M15}. Residue 100 (A→E) was not included in the structure. (*C*) Fluorescent-reporter assay for determining relative amber suppression efficiency in *E. coli*. Bacteria are transformed with a plasmid encoding superfolder-GFP with a stop codon N-terminal to the chromophore. Efficient orthogonal pairs produce larger amounts of aminoacylated-tRNA, resulting in high levels of amber stop-codon readthrough and expression of full-length fluorescent superfolder-GFP. On the other hand, less efficient orthogonal pairs will produce more truncated-sfGFP and less sfGFP fluorescence. (*D*) Fluorescent-reporter assay for mammalian cell amber suppression efficiency, where increased incorporation results in more sfGFP fluorescence while iRFP$_{713}$ serves as a transfection control. (*E*) The chPylRS$_{IPYE}$/tRNA^{M15} pair incorporates BocK more than twice as efficiently as the reported chPylRS$_{IPYE}$/tRNA^{Pyl*} pair in *E. coli.* (*F*) In HEK293T cells, the chPylRS$^{F}_{IPYE}$/tRNA^{M15} pair incorporates PrK 1.4 times more efficiently than the previously reported *Mb*PylRS^{F}/tRNA^{M15} pair, and only slightly more efficiently than chPylRS$_{IPYE}$/tRNA^{Pyl*}. Light and dark gray horizontal regions demonstrate mean incorporation efficiency for *Mb*PylRS^{F}/tRNA^{M15} with 25 and 250 μM PrK, respectively. The striped bar illustrates theoretically perfect (100%) incorporation efficiency.

mutations were identified and this enzyme, chPylRS$_{IPYE}$, outperformed both *Mb*PylRS and *Mm*PylRS in *Escherichia coli* and recently also in mammalian cells (37–39). Additionally, the orthogonal tRNA has been enhanced by increasing its stability and expression levels (tRNA^{Pyl*}) (40) and then further by adjusting regions known to bind elongation factors (tRNA^{M15}) (41).

To date, chPylRS$_{IPYE}$ and tRNA^{M15} have not been paired in either bacterial or mammalian cells, and it is unclear whether the modifications to the tRNA and to the RS would be compatible with one another. To begin answering this question, we evaluated a published structure (42) of the *Mm*PylRS N-terminal domain complexed with tRNA^{Pyl*}. No substantial structural relationships were seen between the regions mutated in chPylRS$_{IPYE}$ and tRNA^{M15}, opening the possibility that the improved RS and tRNA can function together (Fig. 2*B*). Therefore, we tested the compatibility and efficiency of this pair in *E. coli*. chPylRS$_{IPYE}$ was cloned into the pULTRA expression vector (40) along with either tRNA^{Pyl*} or tRNA^{M15}. This GCE plasmid was cotransformed in *E. coli* (BL21-DE3) together with a published pBAD-sfGFP$_{N149*}$ reporter plasmid encoding sfGFP with an amber nonsense mutation at the 149th codon (43). Since this region is upstream of the chromophore, successful GCE results in readthrough of a fluorescent product, while unsuccessful incorporation leads to the expression of a nonfluorescent truncation product (Fig. 2*C*). When paired with tRNA^{M15}, chPylRS$_{IPYE}$ incorporates a standard Boc-lysine test-ncAA an average of 2.3 times more efficiently than when paired with the standard tRNA^{Pyl*}, as judged by expressed full-length sfGFP fluorescence normalized by OD$_{600}$ (Fig. 2*E*). Encouraged by this result, we tested the performance of the chPylRS$_{IPYE}$/tRNA^{M15} pair in mammalian cells. After adding a previously described activity-enhancing active site Tyr→Phe mutation, we compared the incorporation efficiency of the resulting chPylRS$^{F}_{IPYE}$/tRNA^{M15} pair in mammalian cells with that of the highly active *Mb*PylRS^{F}/tRNA^{M15} pair (41, 44). Using a previously described iRFP$_{713}$-sfGFP reporter system (Fig. 2*D*) in HEK293T cells, we found a 1.4 fold improvement in the incorporation of a clickable amino acid with the pair featuring chPylRS$^{F}_{IPYE}$ as compared to the previously reported *Mb*PylRS^{F}/tRNA^{M15} pair (Fig. 2*F*) (34).

Developing the chPylRS$_{2020}$ Enzymes. Unsatisfied with the modest improvement in mammalian cells, we aimed to generate a synthetase that performs better than chPylRS$^{F}_{IPYE}$. Avoiding modification of the binding pocket, so as to prevent disruption of click-ncAA binding, we sought to introduce additional N-terminal mutations. Given previous studies concerning the function of the N-terminal domain, these mutations would be expected to improve the enzyme's binding to and positioning of the tRNA, without affecting ncAA binding. A study parallel

to that which originally identified chPylRS$_{IPYE}$ reported several additional productive N-terminal mutations (42). These mutations were never tested together with the IPYE mutations, and so we examined the effect of each point mutant on the activity of the chPylRS$^{F}_{IPYE}$ enzyme. Several of these modifications were found to substantially improve the incorporation efficiency of a clickable amino acid, N$_{\varepsilon}$-propargyl-L-lysine (PrK, Fig. 3 *A* and *B*). Subsequently, all pairs of the top-three most beneficial mutations were screened, as well as the full set of the three and the originally reported combinations. In this way, an optimized enzyme, chPylRS$^{F}_{2020}$, was identified (Fig. 3*B* and *SI Appendix*, Fig. S4.1). This synthetase incorporated PrK twice as efficiently as the previously reported *Mb*PylRS^{F} at high amino acid concentrations and almost four times as efficiently at low levels of amino acid (Fig. 3*C*). Encouraged by these results, we decided to examine whether the "2020" mutations could improve the incorporation of clickable amino acids for other types of bioorthogonal chemistry, specifically the inverse electron-demand Diels–Alder reaction (iEDDA). To test this hypothesis, the binding pocket mutations from a previously reported *M. barkeri* enzyme that incorporates N$_{\varepsilon}$-bicyclononyne-L-lysine (BCN) (Fig. 3*A*) were added into chPylRS$_{2020}$ (30). The resulting chBCNRS$_{2020}$ enzyme provided a major improvement over the previously published *Mb*BCNRS, incorporating BCN nearly tenfold more efficiently at a low concentration of BCN (Fig. 3*C*). Interestingly, although incorporation efficiency increased at 250 μM BCN, total protein expression decreased, suggesting interference with protein synthesis at higher concentrations (*SI Appendix*, Fig. S4.3). Notably, the 2020 mutations did not confer substantial improvements in incorporation efficiencies of two other iEDDA amino acids (N$_{\varepsilon}$-trans-cyclooct-2-en-L-lysine, N$_{\varepsilon}$-cyclopropene-L-lysine) at the 25- and 250-μM concentrations. However, with these amino acids there was not a substantial difference in incorporation efficiency between conditions with high and low amino acid concentrations, even when using the *M. barkeri* enzyme. This suggests that enzyme kinetics is already saturated for these amino acids at these concentrations (*SI Appendix*, Fig. S4.2). Nevertheless, given that the 2020 mutations enhanced incorporation efficiency in enzymes with two different binding pockets in mammalian cells, it is possible that this mutation set may be transferrable to other reported PylRS enzymes.

To see whether the 2020 mutations also enhance incorporation efficiency in bacteria, chPylRS$^{F}_{2020}$ was inserted into the pULTRA vector encoding tRNA^{M15}. The enzyme incorporated PrK more efficiently than chPylRS$^{F}_{IPYE}$ at 1 mM PrK. Furthermore,

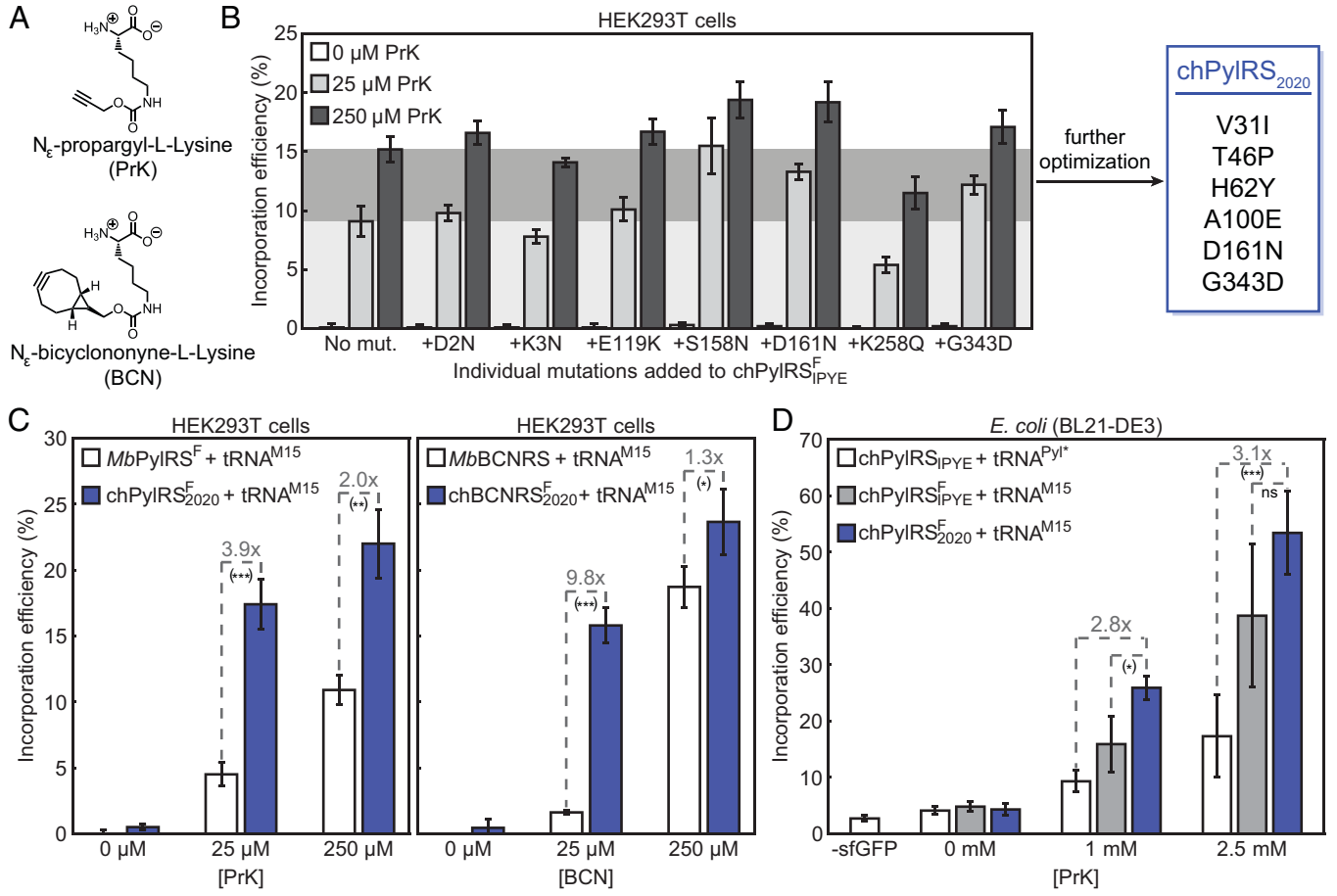

Fig. 3. A newly reported set of synthetases, chPylRS$^{F}_{2020}$ and chBCNRS$_{2020}$, improve incorporation efficiency of clickable amino acids in bacterial and mammalian cells. Bars in plots represent the mean of three biological replicates and error bars show SD between biological replicates. $^{ns}P > 0.05$, $^{*}P < 0.05$, $^{**}P < 0.01$, $^{***}P < 0.001$ (see *SI Appendix*, Fig. S14 for exact *P* values). (*A*) Chemical structures of the clickable amino acids studied in this section. (*B*) Point mutations identified in a previous publication were introduced into chPylRS$^{F}_{IPYE}$ and the incorporation efficiency of the mutant enzymes with tRNA^{M15} was analyzed in cultured HEK293T cells. Beneficial mutations were combinatorically analyzed and the best-performing enzyme, chPylRS$^{F}_{2020}$, included two mutations in addition to IPYE and Y349F. Light and dark gray horizontal regions demonstrate mean incorporation efficiency for chPylRS$^{F}_{IPYE}$/tRNA^{M15} with 25 and 250 μM PrK, respectively. (*C*) chPylRS$_{2020}$/tRNA^{M15} orthogonal pairs incorporate both PrK and BCN several times more effectively than the previously reported *Mb*PylRS/tRNA^{M15} system in HEK293T cells. (*D*) The chPylRS$^{F}_{2020}$/tRNA^{M15} orthogonal pair outperforms chPylRS$^{F}_{IPYE}$/tRNA^{M15} at incorporating PrK in *E. coli* and substantially improves protein expression levels as compared to the published chPylRS$_{IPYE}$/tRNA^{Pyl*} pair.

powered largely by the effects of $tRNA^{M15}$, the $chPylRS^{F}_{2020}$/$tRNA^{M15}$ pair incorporates PrK 3.1 times more efficiently than the published $chPylRS_{IPYE}$/$tRNA^{Pyl*}$ pair (Fig. 3*D*).

Fluorescence Microscopy with $chPylRS^{F}_{2020}$ and $chBCNRS_{2020}$ + $tRNA^{M15}$ Orthogonal Pairs. Motivated by the strongly enhanced incorporation of PrK and BCN via the $chPylRS^{F}_{2020}$ and $chBCNRS_{2020}$ enzymes, we sought to test whether this improvement could increase fluorescence signal in imaging experiments. To answer this question, we incorporated PrK and BCN via $chPylRS^{F}_{2020}$ into a muscarinic G protein-coupled receptor (GPCR), M_2R_{V186*}, a construct which has been previously labeled using GCE (24). This GPCR was expressed in HEK293T cells together with a GCE orthogonal pair and was labeled under live-cell conditions with the switchable fluorophore Alexa Fluor-647, either via chelation-assisted copper-catalyzed azide-alkyne cycloaddition (CuAAC) or iEDDA (Fig. 4*A*). Cells were imaged after fixation. Brighter GPCR labeling was seen for both PrK and BCN incorporation with $chPylRS^{F}_{2020}$ and $chBCNRS_{2020}$ as compared to *Mb*$PylRS^{F}$ and *Mb*BCNRS, respectively (Fig. 4*B* and *SI Appendix*, Figs. S5.1–S5.4).

Asking whether the $chPylRS^{F}_{2020}$/$tRNA^{M15}$ orthogonal pair would also improve fluorescence signal for labeled bacterial proteins, a similar experiment was performed in *E. coli*. A previously reported osmoporin C construct for GCE ($OmpC_{D311*}$) was expressed in BL21-DE3 *E. coli* with several orthogonal pairs (45). As in mammalian cells, the $chPylRS^{F}_{2020}$/$tRNA^{M15}$ pair presented an enhancement over the previously reported pair, $chPylRS_{IPYE}$/$tRNA^{Pyl*}$ (Fig. 4*C* and *SI Appendix*, Figs. S6.1 and S6.2).

Three-Dimensional MINFLUX Fluorescence Imaging of β-Actin in Filopodia Labeled with $chPylRS_{2020}$/$tRNA^{M15}$. Encouraged by the improved labeling efficiencies, we sought to apply our GCE pair for fluorescence imaging at the highest precisions using 3D MINFLUX nanoscopy. Since we aimed to explore whether GCE can be used to tag proteins with minimal label-related changes, we sought to study a tightly packed structure, which may be influenced by bulky tags, such as fluorescent proteins (46). Therefore, we chose to label β-actin, focusing on filopodia, narrow plasma-membrane projections of cells that are formed from β-actin filaments and that have previously been studied by electron tomographic approaches (Fig. 5*A*) (47).

A previously reported $\beta\text{-actin}_{K118*}$ construct was cotransfected with orthogonal pairs featuring the 2020 mutations in U2OS cells (33). Incorporation of PrK, BCN, and two other clickable amino acids was tested. To obtain biological relevance, high label density and low background fluorescence are mandatory. To minimize background, nonfilamentous β-actin monomer was removed via a previously reported cofixation/extraction protocol with glutaraldehyde and Triton X-100 prior to fixation with glutaraldehyde (48). Cells with PrK incorporated into β-actin showed lower background and cleaner protein labeling (higher-contrast images) than those with other ncAAs (*SI Appendix*, Fig. S7.1). Furthermore, PrK is the smallest of these ncAAs (~0.7 nm, *SI Appendix*, section 10), so the $chPylRS^{F}_{2020}$/$tRNA^{M15}$ pair with PrK was used moving forward.

To investigate whether the degree of labeling might be high enough, we labeled $\beta\text{-actin}_{PrK118}$ with the nonswitchable fluorophore picolyl-azide silicon rhodamine and then recorded the samples using STED nanoscopy. Labeling with PrK via our orthogonal synthetase allowed us to routinely obtain STED images, suggesting a substantial labeled fraction of the β-actin (Fig. 5*A*).

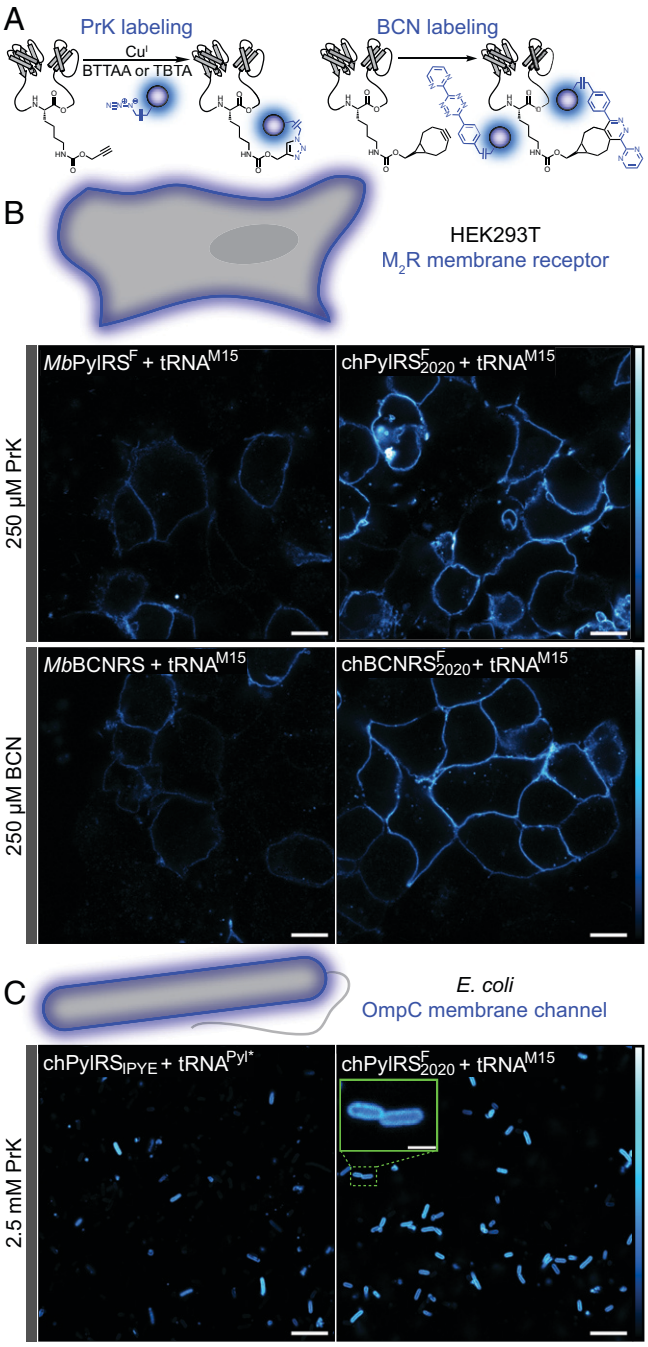

Fig. 4. Incorporation and labeling of clickable ncAAs in mammalian and bacterial membrane proteins. (*A*) PrK-tagged proteins were labeled with chelation-assisted copper-catalyzed azide/alkyne click chemistry using the azide-plus variant of Alexa Fluor-647. BCN-tagged proteins were labeled by inverse electron-demand Diels–Alder chemistry and a tetrazine variant of Alexa Fluor-647. (*B*) With $tRNA^{M15}$, $chPylRS^{F}_{2020}$ greatly enhanced staining of M_2R GPCRs as compared to *Mb*$PylRS^{F}$ when PrK was incorporated at position 186 in the protein. In addition, $chBCNRS_{2020}$ substantially improves the level of labeled M_2R_{BCN186} as compared to *Mb*BCNRS. (*C*) The new $chPylRS^{F}_{2020}$ + $tRNA^{M15}$ pair significantly improves the level of labeled $OmpC_{PrK311}$ as compared to the existing $chPylRS_{IPYE}$ + $tRNA^{Pyl*}$ pair. (Scale bars [*Inset*]: 2 μm. All other scale bars: 10 μm.)

We therefore moved on to image $\beta\text{-actin}_{PrK118}$ using 3D MINFLUX nanoscopy, labeling PrK with a rapidly reacting azide-plus variant of the switchable Alexa Fluor-647 fluorescent dye ($AF647_{Az+}$). Actin filopodia were measured in 3D with spatial precisions (σ) between 1 and 2.5 nm in all directions (Fig. 5*B*) and, after drift correction (*SI Appendix*, Fig. S11.1), were rendered in 3D (Fig. 5*C*). Most measured filopodia were found

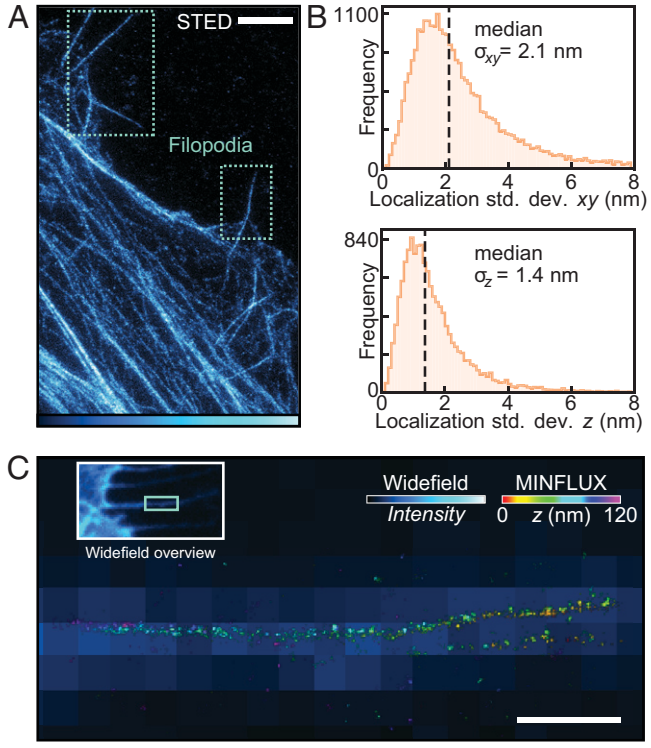

Fig. 5. Superresolution imaging of U2OS filopodia labeled by genetic code expansion. (*A*) STED image of β-actin$_{PrK118}$ labeled with picolyl-azide silicon rhodamine in U2OS cells, highlighting filopodia. (Scale bar: 2 μm.) (*B*) Distributions for the estimated precision of Alexa Fluor-647 localizations from 14 separate MINFLUX measurements of filopodia. (*C*) Overlay of a widefield and corresponding MINFLUX image depicting a representative filopodium that protrudes straight out of the cell. MINFLUX localizations were processed and then rendered by the program Imaris as described in *SI Appendix*, section 1. (Scale bar: 500 nm.)

to be straight projections, with diameters of ∼40 nm. One measurement featured filopodia crossing over one another (Fig. 6*A*). Although still suboptimally labeled, some substructure could be discerned. Toward the base of the assembly, a region can be identified wherein two actin bundles can be resolved as being separated by ∼20 to 50 nm at different points, possibly also twisting around each other (Fig. 6 *A*, *i*–*iii*). A measurement of a kinked filopodium similarly showed actin bundles, which appear to twist around one another (Fig. 6*B*). Filopodia have been shown to kink and twist in response to frictional forces (49–51), so it is possible that internal actin bundles must also coil to allow for such deformations, as has been suggested (51).

We examined the extent to which information about the packing of individual filaments within the filopodia could be extracted at the presently achieved labeling degree. Cryoelectron tomographs of filopodia have shown that, in straight segments, single filaments are separated by ∼12 nm and are mostly parallel, arranged on a triangular lattice (Fig. 7*A*) (47). Given that the combination of the ncAA side chain with the linker on the fluorophore adds only an ∼1.25-nm displacement from the protein backbone (*SI Appendix*, Fig. S10.1), and given the ∼2-nm localization precision of the MINFLUX measurements, such a pattern is right on the limits of what might be visible in the data, particularly given mechanical drift (*SI Appendix*, Fig. S9.1). To begin exploring this possibility, we sliced the measurement data into overlapping 6-nm-thick slices in *z* and selected regions where adjacent actin filaments could be discerned. Several regions with two to three adjacent filaments were identified that featured spacings close to 12 nm (Fig. 7*B* and *SI Appendix*, Fig. S12.1).

Seeking to extend the analysis into the *z* direction, we asked whether molecular distributions consistent with the triangular-lattice pattern might be appreciable. Although the incomplete labeling would likely prevent cross-sectional visualization of the full bundle of actin filaments, thinner regions along the length of the filopodium might be identified. Given that some amount of curvature does exist in the measured filopodia (Fig. 7*C*, *Inset*), their central axis was modeled (*SI Appendix*, Fig. S13.1) and 200-nm-thick cross-sectional slices were analyzed. In several regions across multiple measurements, patterns consistent with the putative packing distribution could be discerned (Fig. 7*D* and *SI Appendix*, Fig. S13.2). These results suggest that the sub-nanometer modification introduced by the PrK amino acid indeed preserves the delicate bundling structure of actin filaments in filopodia.

Discussion

Given the single-nanometer localization precisions achieved by MINFLUX and related molecular-scale fluorescence nanoscopy

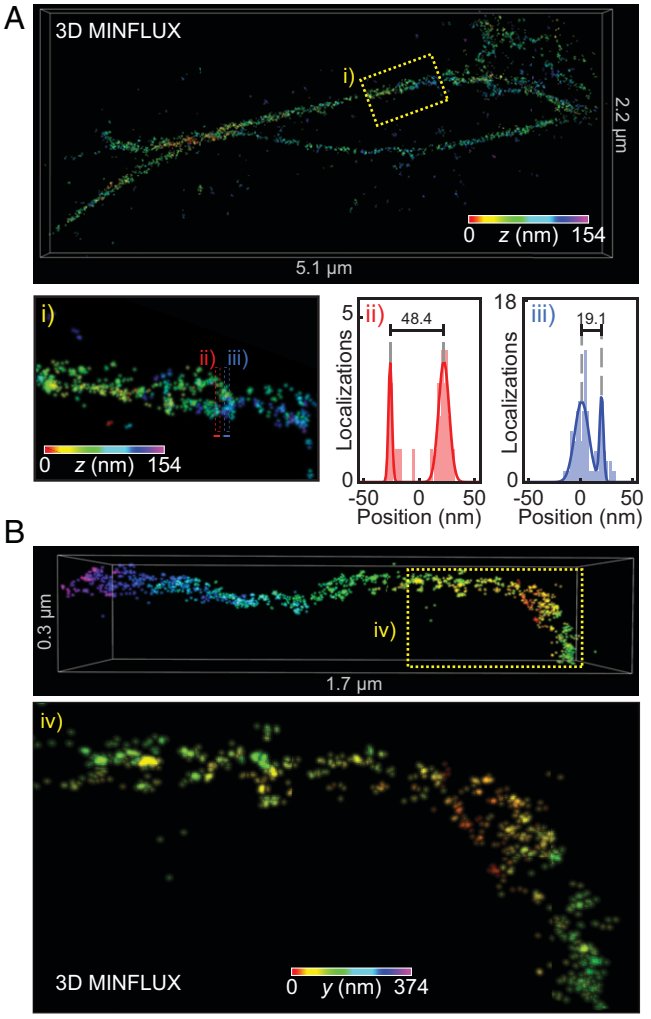

Fig. 6. Inspection of U2OS filopodia measured by MINFLUX nanoscopy. (*A*) MINFLUX image showing crossing filopodia. (*i*) Expanded view of the same region labeled at the *Top*. Substructure can be seen with actin bundles crossing around each other. (*ii*/*iii*) Cross-sectional localization histograms from the corresponding regions shown in *i*, demonstrating measured separations as close as ∼20 nm and up to ∼50 nm between the two bundles. (*B*) MINFLUX measurement of a kinked filopodium. (*iv*) Expanded view of the region boxed in yellow, depicting actin bundles that appear to wrap around each other.

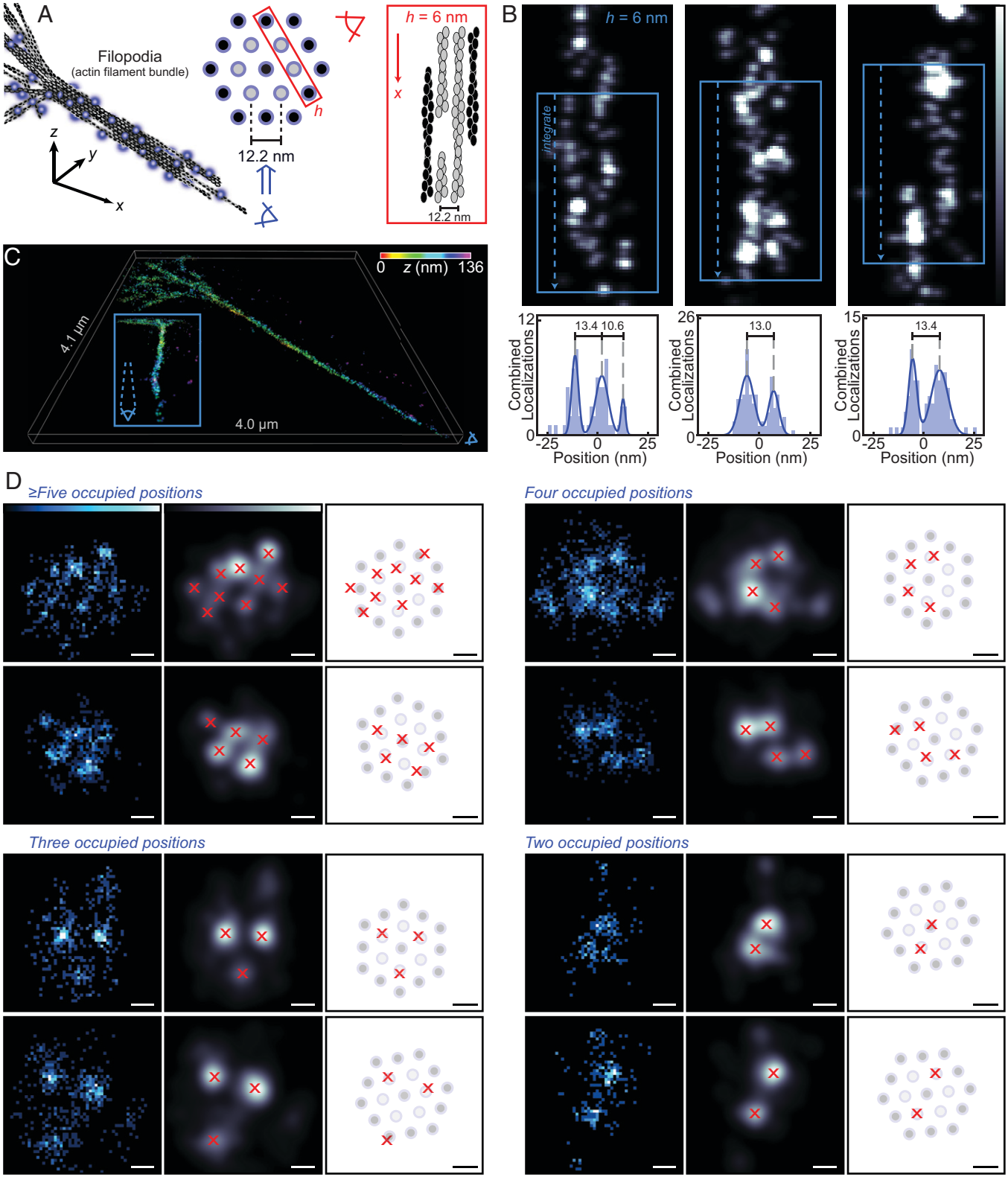

Fig. 7. Cross-sectional analysis of filopodia measured by 3D MINFLUX nanoscopy. (*A*) Within filopodia, actin filaments are expected to be arranged on a triangular lattice with 12.2 ± 0.9(σ) nm spacing between nearest neighbors. (*B*) Blue box widths = 60 nm. Two-dimensional intensity projections of adjacent actin filaments within filopodia, discerned in 6-nm-thick slices of the 3D localizations. Histograms calculated from drift-corrected localization data. Images shown are processed via Gaussian blurs in *yz* and *xy* (σ = 1.5 nm). (*C*) 3D MINFLUX rendering of a filopodium color coded in *z*. The *Inset* shows the same dataset from an alternate angle, demonstrating the existence of bending along the length of filopodia. (*D*) After modeling the central axis of filopodia (*SI Appendix*, section 13), the actin filament bundling pattern can be resolved in multiple 200-nm projections of 3D MINFLUX data along the filopodia axis. Many projections correspond well with the lattice on which the filaments should be positioned. Representative images featuring different lattice occupancies are shown (*Left*: intensity image from localization data; *Center*: Gaussian blur [σ = 3.5 nm]; and *Right*: overlay of peaks on theoretical lattice). (Scale bars: 12 nm.)

techniques, we optimized a labeling system that introduces fluorophore-to-target offsets at or below those length scales. Systematic optimization of a PylRS/tRNA pair allowed us to develop an enzyme, chPylRS$^{F}_{2020}$, which improves the incorporation of clickable amino acids in both mammalian cells and *E. coli*. Paired with tRNA^{M15}, this enzyme enhanced labeling for fluorescent imaging of target proteins and allowed for robust STED and MINFLUX imaging of β-actin. Subsequent analysis of 3D MINFLUX filopodia measurements identified localization patterns that can be rationalized to originate from an underlying triangular filament bundling pattern, with an average nearest-neighbor distance of around 12 nm. Although the fluorophore labeling degree was not sufficient to independently prove the bundling geometry, visualization of localization patterns consistent with structural elements that were previously only accessible via cryogenic imaging methods highlights the potential of molecular-scale fluorescence imaging when paired with minimally displacing labeling tags.

Despite this, the density of localized molecules can be advanced, and further evolution of the MINFLUX acquisition sequence should additionally improve the proportion of active labels that are detected. The labeling itself must also still be substantially improved, enhancing signal and reducing background. Incorporation efficiency might be further increased by introducing even more tRNA copies or by also expressing a previously reported engineered eukaryotic release factor (52). In our experiments, protein-of-interest plasmid with the UAG stop codon was transiently transfected into cells alongside the GCE plasmid. In β-actin labeling, the tagged protein must compete with the cell's endogenous wild-type actin for incorporation into filaments, so knockdown of endogenous protein (e.g., via siRNA) is likely to enhance label density. With the newly optimized GCE pair reported in this study, it should even be possible to stably replace an essential endogenous protein such as actin with the tagged version via stable CRISPR-based genetic code modification.

Due to the presence of background staining in GCE-labeled samples, high-quality superresolution imaging has been practically limited to dense structures (such as the cytoskeleton) and membrane proteins. Some of this background has previously been shown to originate from labeling of aminoacylated-tRNAs (33, 34, 36) and from the suppression of endogenous mRNA amber codons in the cells (*SI Appendix*, Fig. S7.1) (33, 34, 36). Spatial sequestration of GCE machinery into designer membraneless organelles has enabled amber suppression of selected mRNAs, removing ncAA incorporation into endogenous proteins (53). Furthermore, recent demonstration of membraneless organelle formation within ∼100-nm zones of selected cell membranes shows that GCE machinery can be spatially positioned at known regions within cells (54). In this way, directing ncAA incorporation machinery exclusively for proteins of interest at specified positions in space away from imaging targets, or developing a method to eliminate signal from labeled tRNAs, might enable nanometer-scale fluorescence imaging of low-abundance protein targets in the cytosol and other compartments.

Despite these present limitations, our results show that the pairing of GCE and MINFLUX holds considerable promise as a powerful method for the imaging of small and sensitive biological structures at the molecular scale.

Materials and Methods

A detailed description of the materials and experimental methods, including sample preparation procedures, measurements of relative noncanonical amino acid incorporation efficiencies, mutation analysis and generation of chPylRS variants, and the MINFLUX data acquisition and analysis are provided in *SI Appendix, SI Materials and Methods*.

Data Availability. All study data are included in the article and/or *SI Appendix*.

ACKNOWLEDGMENTS. T.S.M. was the recipient of a 2019–2020 Fulbright Scholarship. We are grateful to Dr. Alexey Butkevich (Max Planck Institute for Medical Research, Heidelberg) for providing the picolyl-azide silicon rhodamine dye.

Author affiliations: [a]Department of NanoBiophotonics, Max Planck Institute for Multidisciplinary Sciences, Göttingen, 37077, Germany; and [b]Department of Optical Nanoscopy, Max Planck Institute for Medical Research, Heidelberg, 69120, Germany

1. S. J. Sahl, S. W. Hell, S. Jakobs, Fluorescence nanoscopy in cell biology. *Nat. Rev. Mol. Cell Biol.* **18**, 685–701 (2017).
2. S. W. Hell, J. Wichmann, Breaking the diffraction resolution limit by stimulated emission: Stimulated-emission-depletion fluorescence microscopy. *Opt. Lett.* **19**, 780–782 (1994).
3. E. Betzig *et al.*, Imaging intracellular fluorescent proteins at nanometer resolution. *Science* **313**, 1642–1645 (2006).
4. M. J. Rust, M. Bates, X. Zhuang, Sub-diffraction-limit imaging by stochastic optical reconstruction microscopy (STORM). *Nat. Methods* **3**, 793–795 (2006).
5. S. T. Hess, T. P. K. Girirajan, M. D. Mason, Ultra-high resolution imaging by fluorescence photoactivation localization microscopy. *Biophys. J.* **91**, 4258–4272 (2006).
6. K. Xu, G. Zhong, X. Zhuang, Actin, spectrin, and associated proteins form a periodic cytoskeletal structure in axons. *Science* **339**, 452–456 (2013).
7. R. Barth, K. Bystricky, H. A. Shaban, Coupling chromatin structure and dynamics by live super-resolution imaging. *Sci. Adv.* **6**, eaaz2196 (2020).
8. M. G. M. Velasco *et al.*, 3D super-resolution deep-tissue imaging in living mice. *Optica* **8**, 442–450 (2021).
9. F. Balzarotti *et al.*, Nanometer resolution imaging and tracking of fluorescent molecules with minimal photon fluxes. *Science* **355**, 606–612 (2017).
10. M. Weber *et al.*, MINSTED fluorescence localization and nanoscopy. *Nat. Photonics* **15**, 361–366 (2021).
11. K. C. Gwosch *et al.*, MINFLUX nanoscopy delivers 3D multicolor nanometer resolution in cells. *Nat. Methods* **17**, 217–224 (2020).
12. J. K. Pape *et al.*, Multicolor 3D MINFLUX nanoscopy of mitochondrial MICOS proteins. *Proc. Natl. Acad. Sci. U.S.A.* **117**, 20607–20614 (2020).
13. R. Schmidt *et al.*, MINFLUX nanometer-scale 3D imaging and microsecond-range tracking on a common fluorescence microscope. *Nat. Commun.* **12**, 1478 (2021).
14. A. Keppler *et al.*, A general method for the covalent labeling of fusion proteins with small molecules in vivo. *Nat. Biotechnol.* **21**, 86–89 (2003).
15. G. V. Los *et al.*, HaloTag: A novel protein labeling technology for cell imaging and protein analysis. *ACS Chem. Biol.* **3**, 373–382 (2008).
16. A. Gautier *et al.*, An engineered protein tag for multiprotein labeling in living cells. *Chem. Biol.* **15**, 128–136 (2008).
17. S. M. Früh *et al.*, Site-specifically-labeled antibodies for super-resolution microscopy reveal *in situ* linkage errors. *ACS Nano* **15**, 12161–12170 (2021).
18. M. Y. Lobanov, E. I. Furletova, N. S. Bogatyreva, M. A. Roytberg, O. V. Galzitskaya, Library of disordered patterns in 3D protein structures. *PLOS Comput. Biol.* **6**, e1000958 (2010).
19. V. N. Uversky, The most important thing is the tail: Multitudinous functionalities of intrinsically disordered protein termini. *FEBS Lett.* **587**, 1891–1901 (2013).
20. L. Xue, I. A. Karpenko, J. Hiblot, K. Johnsson, Imaging and manipulating proteins in live cells through covalent labeling. *Nat. Chem. Biol.* **11**, 917–923 (2015).
21. D. Wildanger, R. Medda, L. Kastrup, S. W. Hell, A compact STED microscope providing 3D nanoscale resolution. *J. Microsc.* **236**, 35–43 (2009).
22. F. Opazo *et al.*, Aptamers as potential tools for super-resolution microscopy. *Nat. Methods* **9**, 938–939 (2012).
23. J. Z. Rappoport, S. M. Simon, A functional GFP fusion for imaging clathrin-mediated endocytosis. *Traffic* **9**, 1250–1255 (2008).
24. R. Serfling *et al.*, Quantitative single-residue bioorthogonal labeling of G protein-coupled receptors in live cells. *ACS Chem. Biol.* **14**, 1141–1149 (2019).
25. R. Köchl *et al.*, The signal peptide of the G protein-coupled human endothelin B receptor is necessary for translocation of the N-terminal tail across the endoplasmic reticulum membrane. *J. Biol. Chem.* **277**, 16131–16138 (2002).
26. K. Afitska, A. Fucikova, V. V. Shvadchak, D. A. Yushchenko, Modification of C terminus provides new insights into the mechanism of α-synuclein aggregation. *Biophys. J.* **113**, 2182–2191 (2017).
27. J. W. Chin *et al.*, An expanded eukaryotic genetic code. *Science* **301**, 964–967 (2003).
28. K. Lang, J. W. Chin, Cellular incorporation of unnatural amino acids and bioorthogonal labeling of proteins. *Chem. Rev.* **114**, 4764–4806 (2014).
29. D. P. Nguyen *et al.*, Genetic encoding and labeling of aliphatic azides and alkynes in recombinant proteins via a pyrrolysyl-tRNA Synthetase/tRNA(CUA) pair and click chemistry. *J. Am. Chem. Soc.* **131**, 8720–8721 (2009).
30. K. Lang *et al.*, Genetic encoding of bicyclononynes and trans-cyclooctenes for site-specific protein labeling in vitro and in live mammalian cells via rapid fluorogenic Diels-Alder reactions. *J. Am. Chem. Soc.* **134**, 10317–10320 (2012).
31. J. E. Hoffmann *et al.*, Highly stable trans-cyclooctene amino acids for live-cell labeling. *Chemistry* **21**, 12266–12270 (2015).
32. I. Nikić, J. H. Kang, G. E. Girona, I. V. Aramburu, E. A. Lemke, Labeling proteins on live mammalian cells using click chemistry. *Nat. Protoc.* **10**, 780–791 (2015).

33. C. Uttamapinant *et al.*, Genetic code expansion enables live-cell and super-resolution imaging of site-specifically labeled cellular proteins. *J. Am. Chem. Soc.* **137**, 4602–4605 (2015).
34. I. Nikić *et al.*, Debugging eukaryotic genetic code expansion for site-specific click-PAINT super-resolution microscopy. *Angew. Chem. Int. Ed. Engl.* **55**, 16172–16176 (2016).
35. F. Neubert *et al.*, Bioorthogonal click chemistry enables site-specific fluorescence labeling of functional NMDA receptors for super-resolution imaging. *Angew. Chem. Int. Ed. Engl.* **57**, 16364–16369 (2018).
36. N. Aloush *et al.*, Live cell imaging of bioorthogonally labelled proteins generated with a single pyrrolysine tRNA gene. *Sci. Rep.* **8**, 14527 (2018).
37. D. I. Bryson *et al.*, Continuous directed evolution of aminoacyl-tRNA synthetases. *Nat. Chem. Biol.* **13**, 1253–1260 (2017).
38. Y. Chen *et al.*, Addition of isocyanide-containing amino acids to the genetic code for protein labeling and activation. *ACS Chem. Biol.* **14**, 2793–2799 (2019).
39. W. Zhou, J. S. Wesalo, J. Liu, A. Deiters, Genetic code expansion in mammalian cells: A plasmid system comparison. *Bioorg. Med. Chem.* **28**, 115772 (2020).
40. A. Chatterjee, S. B. Sun, J. L. Furman, H. Xiao, P. G. Schultz, A versatile platform for single- and multiple-unnatural amino acid mutagenesis in *Escherichia coli*. *Biochemistry* **52**, 1828–1837 (2013).
41. R. Serfling *et al.*, Designer tRNAs for efficient incorporation of non-canonical amino acids by the pyrrolysine system in mammalian cells. *Nucleic Acids Res.* **46**, 1–10 (2018).
42. T. Suzuki *et al.*, Crystal structures reveal an elusive functional domain of pyrrolysyl-tRNA synthetase. *Nat. Chem. Biol.* **13**, 1261–1266 (2017).
43. S. J. Miyake-Stoner *et al.*, Generating permissive site-specific unnatural aminoacyl-tRNA synthetases. *Biochemistry* **49**, 1667–1677 (2010).
44. T. Yanagisawa *et al.*, Multistep engineering of pyrrolysyl-tRNA synthetase to genetically encode N(epsilon)-(o-azidobenzyloxycarbonyl) lysine for site-specific protein modification. *Chem. Biol.* **15**, 1187–1197 (2008).
45. K. Kipper *et al.*, Application of noncanonical amino acids for protein labeling in a genomically recoded *Escherichia coli*. *ACS Synth. Biol.* **6**, 233–255 (2017).
46. B. J. Belin, L. M. Goins, R. D. Mullins, Comparative analysis of tools for live cell imaging of actin network architecture. *Bioarchitecture* **4**, 189–202 (2014).
47. M. Jasnin *et al.*, Three-dimensional architecture of actin filaments in Listeria monocytogenes comet tails. *Proc. Natl. Acad. Sci. U.S.A.* **110**, 20521–20526 (2013).
48. L. Gu *et al.*, Molecular resolution imaging by repetitive optical selective exposure. *Nat. Methods* **16**, 1114–1118 (2019).
49. N. Leijnse, L. B. Oddershede, P. M. Bendix, Helical buckling of actin inside filopodia generates traction. *Proc. Natl. Acad. Sci. U.S.A.* **112**, 136–141 (2015).
50. M. M. A. E. Claessens, C. Semmrich, L. Ramos, A. R. Bausch, Helical twist controls the thickness of F-actin bundles. *Proc. Natl. Acad. Sci. U.S.A.* **105**, 8819–8822 (2008).
51. N. Leijnse *et al.*, Filopodia rotate and coil by actively generating twist in their actin shaft. *Nat. Commun.* **13**, 1636 (2022).
52. W. H. Schmied, S. J. Elsässer, C. Uttamapinant, J. W. Chin, Efficient multisite unnatural amino acid incorporation in mammalian cells via optimized pyrrolysyl tRNA synthetase/tRNA expression and engineered eRF1. *J. Am. Chem. Soc.* **136**, 15577–15583 (2014).
53. C. D. Reinkemeier, G. E. Girona, E. A. Lemke, Designer membraneless organelles enable codon reassignment of selected mRNAs in eukaryotes. *Science* **363**, eaaw2644 (2019).
54. C. D. Reinkemeier, E. A. Lemke, Dual film-like organelles enable spatial separation of orthogonal eukaryotic translation. *Cell* **184**, 4886–4903.e21 (2021).